Coastal Engineering 164 (2021) 103820

Contents lists available at ScienceDirect

Coastal Engineering

journal homepage: http://www.elsevier.com/locate/coastaleng

Modelling wave attenuation by quasi-flexible coastal vegetation

Thomas J. van Veelen *, Harshinie Karunarathna, Dominic E. Reeve

Energy and Environment Research Group, Zienkiewicz Centre for Computational Engineering, Swansea University, SA1 8EN, Swansea, United Kingdom

ARTICLE INFO

Keywords:
Flexible vegetation
Nature-based coastal defences
Vegetation modelling
Wave damping
Salt marshes

ABSTRACT

Coastal vegetation such as seagrass fields, salt marshes, and mangroves, contributes to coastal defence by damping incoming waves. Yet, plant species differ in flexibility due to which they interact differently with incoming waves and damp waves to a variable degree. Current wave damping models struggle to balance accuracy against computational costs when accounting for wave-vegetation interactions. Instead, they often rely on a plant-specific calibration of the drag coefficient, which limits their application across plant species. Here we show, using novel simultaneous experimental data of wave damping, water velocities and stem motion, that wave damping by quasi-flexible cylindrical vegetation is controlled by the relative velocity between water and vegetation at the upright bottom section of a stem. For the quasi-flexible vegetation conditions considered in this manuscript ($L > 1.4$ and $Ca < 700$), our experimental evidence justifies the application of a model based on the Euler-Bernoulli beam theory to estimate plant motion. Building on the solution of plant motion, we simulate wave damping over flexible vegetation fields through a new work factor. Our model successfully predicts damping of regular waves by rigid and flexible artificial vegetation, and real *S. Anglica*, *P. Maritima* and *E. Athericus* plants in the right order of magnitude under medium and high energy wave conditions. The simulated wave damping is directly linked to vegetation and wave conditions and does not require a plant-specific calibration of the drag coefficient. It is anticipated that the model will be of wide practical use in simulating wave damping by quasi-flexible cylindrical coastal vegetation across large areas with diverse plant species and wave conditions.

1. Introduction

Coastal vegetation is found around the globe in the form of seagrass fields, kelp forests, salt marshes and mangrove forests (Mullarney et al., 2018). The vegetation across and within these habitats differs significantly, ranging from flexible grasses to rigid shrubs and trees. When vegetation is present on or seaward of the coastline, it interacts with incoming waves (Leonardi et al., 2018).

Vegetation contributes to coastal protection by damping incoming waves (Jadhav et al., 2013; Losada et al., 2016; Möller et al., 2014). When waves travel over vegetation, energy is dissipated due to the work done by wave forces on plants (Dalrymple et al., 1984). This can significantly reduce wave impact on beaches and hard structures, lowering their construction and maintenance costs (Temmerman et al., 2013; Vuik et al., 2016). Additionally, vegetation reduces storm surge propagation, stabilises shorelines during storms, and contributes to sediment capture, carbon storage and recreational opportunities outside storm events (Bouma et al., 2014; Fagherazzi et al., 2012; Stark et al., 2016; Sutton-Grier et al., 2015; Wamsley et al., 2009).

Stem motion of flexible vegetation can impact wave damping significantly as has been demonstrated in experimental (Luhar et al., 2017; Paul et al., 2016; Riffe et al., 2011) and computational studies (Luhar and Nepf, 2016; Mullarney and Henderson, 2010). Vegetation species are broadly classified as rigid or flexible. Rigid vegetation, like woody shrubs, does not move over a wave cycle, whereas flexible vegetation, like thin grass, sways as its rigidity is insufficient to resist stem bending. The excursion of flexible species increases when its flexural rigidity decreases or wave forces increase (Luhar et al., 2017). As stem bending increases, the plant frontal area and the relative velocity between water and stem decrease (Méndez et al., 1999; Paul et al., 2016). Both limit the wave forces on the plant and may reduce wave damping by up to 50–70% (Luhar et al., 2017; Mullarney and Henderson, 2010; Riffe et al., 2011; van Veelen et al., 2020). However, as the interaction between plant motion and wave forces is reciprocal,

* Corresponding author.
E-mail addresses: thomas.vanveelen@swansea.ac.uk (T.J. van Veelen), h.u.karunarathna@swansea.ac.uk (H. Karunarathna), d.e.reeve@swansea.ac.uk (D.E. Reeve).

https://doi.org/10.1016/j.coastaleng.2020.103820
Received 25 September 2019; Received in revised form 9 November 2020; Accepted 21 November 2020
Available online 26 November 2020
0378-3839/© 2020 The Author(s). Published by Elsevier B.V. This is an open access article under the CC BY license (http://creativecommons.org/licenses/by/4.0/).

quantifying wave damping over flexible species poses a challenge.

Computational models can be a valuable tool to quantify wave damping for variable vegetation properties. For rigid vegetation, Dalrymple et al. (1984) simplified vegetation fields to arrays of rigid cylinders on a flat bottom and assumed validity of linear wave theory to model damping of monochromatic waves. Under these assumptions, they demonstrated that wave damping is dominated by drag, and wave heights reduce proportionally to the distance travelled over vegetation. Using the same modelling framework, Mendez and Losada (2004) proposed to calibrate the drag coefficient to include the effect of stem motion. Their model was successfully applied in field (Bradley and Houser, 2009; Garzon et al., 2019; Jadhav et al., 2013) and flume studies (Anderson and Smith, 2014; Augustin et al., 2009; Koftis et al., 2013; Losada et al., 2016; Möller et al., 2014; van Veelen et al., 2020), but the calibrated drag coefficients vary widely between plant species and test conditions (Mullarney et al., 2018; Vuik et al., 2016), and when vegetation conditions change (Schulze et al., 2019). Thus, site-specific calibration for each coastal habitat is required.

Alternatively, an effective stem length can be employed to include the effect of stem bending in a rigid vegetation model. The effective stem length is the height of a rigid stem that generates equal drag as that of the (longer) flexible stem (Luhar and Nepf, 2011). Paul et al. (2016) proposed using observed frontal area as the effective vegetation length, based on experiments with lexaan strips. Instead, Luhar et al. (2017) fitted an analytical model for the effective length of flexible seagrass based on a scaling analysis of the equations of stem motion but suggested that different fits for different species are required. Their model was expanded to a predictive model for wave damping by Lei and Nepf (2019), who further discriminated between rigid and flexible stem sections and introduced a new fit for the effective stem length.

Other models have included vegetation motion explicitly by modelling stems as flexible rods. Mendez et al. (Méndez et al., 1999) solved the excursion of the tip using stem-averaged velocities and a linearised drag force in an idealised model. Vertical variations in the velocity profile were included by Mullarney and Henderson (2010) and the buoyancy force was included in Henderson (2019). However, these models are limited to stems with small deflections. Alternatively, complex computational models included friction, inertia and buoyancy forces to solve stem motion under strong plant bending for individual stems (Leclercq and de Langre, 2018; Luhar and Nepf, 2016) and vegetation fields (Chen and Zou, 2019; Maza et al., 2013). However, the computational cost for these models is high, which makes them unsuitable for large areas.

The various modelling approaches show a trade-off between complexity, accuracy, computational cost, and applicability, but the optimal balance for practical cases remains unclear. Simple models can be easily applied, but require site and plant-specific calibration. Alternatively, complex models add processes which can reduce the variation in calibration, but at a computational cost and potentially increasing model errors. Therefore, the accuracy gains by including additional mechanisms must be carefully weighed against the extra computational costs. Furthermore, no complex model has been successfully validated across multiple species of real vegetation that differ in flexibility.

In the present study, we aim to provide a novel versatile mathematical modelling framework for wave damping over coastal vegetation under quasi-flexible vegetation conditions. Quasi-flexible vegetation conditions are defined as flexible vegetation that does not fold over or fully extent during a wave cycle. A balance between complexity and applicability is obtained by including only the key mechanisms involved in the wave-vegetation interaction. These mechanisms are identified by, for the first time, combining experimental data of wave damping, wave velocity fields, and plant motion. Based on the key physics, we develop a new modelling framework with applicability across cylindrical vegetation species and hydrodynamic conditions without the need for plant-specific calibration.

This manuscript is structured as follows: Section 2 discusses the wave-vegetation interaction. Section 3 presents and discusses the novel experimental data with the aim of justifying model assumptions. The modelling framework is described in Section 4 and validated in Section 5. Finally, conclusions are provided in Section 6.

2. Theoretical background

2.1. Coordinate system

Let us define a coordinate system at canopy-scale (Fig. 1a), where waves travel over a vegetation field on top of a flat bed. The direction of wave propagation is normal to the canopy and parallel to the x-axis with $x = 0$ at the upstream edge of the vegetation. The z-axis describes vertical position with respect to the water column such that $z = 0$ depicts the still water surface and $z = -h$ the bed level. The waves are modelled by their height $H(x)$, period T and velocity field $U(x,z,t) = u + iw$, where the real and complex parts denote the horizontal and vertical dimensions respectively.

A single stem in the canopy is modelled as a cylinder with height h_v, diameter b_v, and flexural rigidity EI_v. Cylinders are an accepted geometry for coastal vegetation types such as salt marsh grasses (Jadhav et al., 2013; Rupprecht et al., 2017), mangrove branches (Strusińska-Correia et al., 2013) and coral (Lowe et al., 2005). Stem density n_v defines the number of stems per unit ground area. We introduce a plant-scale coordinate system to define stem motion (Fig. 1b). Along-stem coordinate s is defined such that $s = 0$ is the root and $s = h_v$ is the tip of the stem. Stem posture $X(s,t) = x_v + iz_v$ follows the complex coordinate system. The stem moves at velocity $U_{veg} = \partial X/\partial t$ and its bending with respect to an upright stem is defined by bending angle $\theta(s,t)$. Finally, we define wave velocities $U_s(s,t) = u_s + iw_s$ and forces $F(s,t) = F_x + iF_z$ at the stem (Fig. 1c).

Dimensionless parameters will be employed for all variables throughout this manuscript (denoted by asterisks). We introduce scaled coordinates

$$x_* = \frac{x}{A_w},\ z_* = \frac{z}{h_v},\ s_* = \frac{s}{h_v},\ t_* = t\omega, \tag{1}$$

and quantities

$$X_* = \frac{X}{h_v},\ H_* = \frac{H}{h}, U_* = \frac{U}{u_c},\ U_{veg*} = \frac{U_{veg}}{u_c},\ F_* = \frac{F}{\rho b_v u_c^2}. \tag{2}$$

Herein, $\omega = 2\pi/T$ is the wave angular frequency, u_c is the velocity scale, $A_w = u_c/\omega$ is the typical wave excursion length, and $\rho = 1000$ kg/m^3 is the water density. u_c is defined as the amplitude of the horizontal wave orbital motion (Hu et al., 2014) according to

$$u_c = \frac{1}{2}\left(u_f + u_b\right) \tag{3}$$

where u_f is the peak forward velocity, u_b is the peak backward velocity, and $\nu = 10^{-6}$ m^2/s is the kinematic viscosity of water. u_f and u_b may be measured or based on linear wave theory. Hu et al. (2014) measured velocities halfway of the water column, which was between 1/3 and 2/3 of the vegetation height. However, it is more appropriate to define the velocity scale relative to the vegetation height, rather than the water column, for moving vegetation. Therefore, we consider the velocities halfway the vegetation height, which is the average of the height range used in Hu et al. (2014). Furthermore, we introduce two dimensionless quantities that control the wave-vegetation interaction for flexible vegetation (Luhar et al., 2017): the Cauchy number

$$Ca = \frac{\rho b_v u_c^2 h_v^3}{EI_v} \tag{4}$$

being the ratio between wave forces and stem stiffness, and the excursion ratio

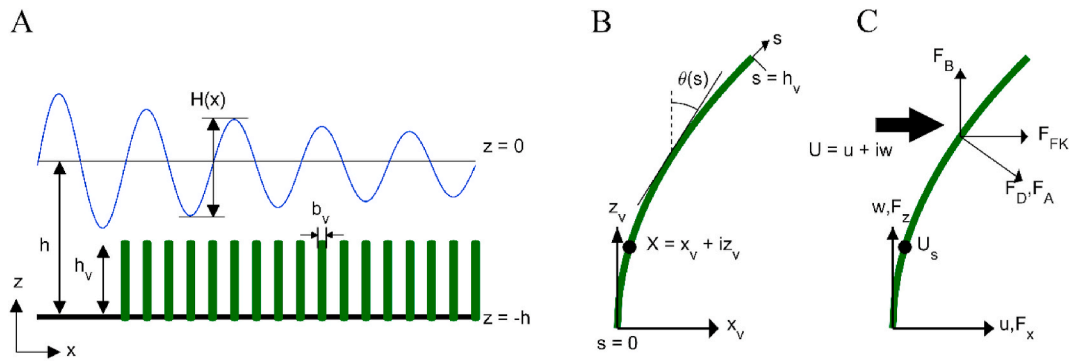

Fig. 1. Definition sketches of the coordinate system of the wave-vegetation interface at the (A) canopy and (B) plant scales. (C) shows the velocities and forces at the plant scale.

$$L = \frac{h_v}{A_w} \tag{5}$$

being the ratio between stem length and wave excursion.

2.2. Wave-vegetation interaction

Vegetation interacts with dynamic forces induced by waves and the static buoyancy force (Fig. 1c). The interaction is one-way for rigid vegetation and two-way for flexible vegetation. We consider three wave-induced forces that act on vegetation. These are given per unit stem length: the drag force;

$$F_{D^*} = \frac{1}{2} C_D |u_{rn^*}| u_{rn^*} e^{-i\theta}, \tag{6}$$

the added mass force;

$$F_{A^*} = \frac{1}{2} C_A \frac{\pi^2}{KC} \frac{\partial u_{rn^*}}{\partial t_*} e^{-i\theta}, \tag{7}$$

the Froude-Krylov force;

$$F_{FK^*} = \frac{1}{2} \frac{\pi^2}{KC} \frac{\partial U_{s^*}}{\partial t_*}. \tag{8}$$

Herein, $u_{rn^*} = \Re(U_{r^*} e^{i\theta})$ and $u_{rp^*} = \Im(U_{r^*} e^{i\theta})$ are the stem-normal and stem-parallel components of the relative velocity between water and stem $U_{r^*} = U_{s^*} - U_{veg^*}$. C_D and C_A are coefficients for drag and added mass respectively and $KC = u_c T / b_v$ is the Keulegan-Carpenter number. The drag coefficient

$$C_D = \left(\frac{730}{Re}\right)^{1.37} + 1.04 \tag{9}$$

was derived via direct force measurements on a field of rigid cylinders in the range $300 < Re < 4700$ by Hu et al. (2014), where $Re = u_c b_v / \nu$ is the vegetation Reynolds number. Although KC may also be a strong predictor for C_D (Chen et al., 2018; Keulegan and Carpenter, 1958; Ozeren et al., 2014), Rehas been selected in this study as Eq. (9) was derived via direct force measurements. The drag coefficient is commonly calibrated to include the effect of vegetation swaying (e.g. Mendez and Losada, 2004) but in this study we include plant motion explicitly such that Eq. (9) is applied to all vegetation types in this study. $C_A = 12.63 KC^{0.0583} - 15.09$ satisfies empirical data by Keulegan and Carpenter (1958) for $KC \geq 20$. We note that their C_M equals $C_A + 1$ in this study as we define the added mass and Froude-Krylov forces separately (Dean and Dalrymple, 1991). The friction force, based on Zeller et al. (2014), is of negligible magnitude for the conditions considered here (Re = 570–1500) and therefore omitted.

The magnitude of F_{A^*} and F_{FK^*} relative to F_{D^*} is controlled by the ratio $\pi^2 / (KC|u_{rn^*}|)$. KC is of the order $O(10^2)$ for conditions considered in this study as is realistic for field conditions (Jadhav et al., 2013). In case of rigid vegetation, $|u_{rn^*}| = |u_{s^*}| = O(10^0)$ and the relative magnitude of F_{A^*} and F_{FK^*} is of order $O(10^{-1})$. The same scaling argument has also been employed for flexible vegetation (e.g. Mullarney and Henderson, 2010), but when the relative velocity reduces due to vegetation swaying, F_{A^*} and F_{FK^*} may be of similar magnitude as F_{D^*}. Therefore, we do consider F_{A^*} and F_{FK^*} at this stage of our analysis. Finally, the net buoyant force

$$F_{B^*} = \frac{1}{4} \pi (\rho' - 1) \frac{g b_v}{u_c^2} i \tag{10}$$

is not exerted by waves but can modify plant posture (Zeller et al., 2014). It features g = 9.81 m/s^2 as the gravitational acceleration and $\rho' = \rho_v / \rho$ as the ratio between the vegetation density (ρ_v) and the water density.

Swaying by flexible vegetation affects the magnitude and direction of the wave forces (Eqs. (6)–(8)). We consider inextensible stems, homogeneous cylindrical cross-sections, homogeneous flexural rigidity, and no interaction between stems. Instead, the sheltering of downstream vegetation can be included through the velocity scale (Eq. (3)). Under these conditions, plant motion is controlled by the force balance (Luhar and Nepf, 2016; Mullarney and Henderson, 2010), according to

$$\frac{1}{2} \frac{\pi^2}{KC} \rho' Ca \frac{\partial U_{veg^*}}{\partial t_*} + \left(\frac{\partial^3 \theta}{\partial s_*^3} - i \frac{\partial \theta}{\partial s_*} \frac{\partial^2 \theta}{\partial s_*^2} \right) e^{-i\theta} = Ca \left(F_{D^*} + F_{A^*} + F_{FK^*} + F_{B^*} \right). \tag{11}$$

The first term on the left-hand side is the stem inertia and the second term expresses bending resistance. The wave and buoyancy forces control plant motion via the forcing term on the right-hand side. Conversely, plant motion controls the direction and the magnitude of the wave forces. This two-way interaction between wave forces and stem motion poses the main challenge in solving wave forces on flexible vegetation. Therefore, our experiments, described in Section 3, aim to identify the key physical interactions relevant to wave damping to justify simplifications of Eq. (11). Specifically, we will investigate the relative magnitude of F_{A^*} and F_{FK^*}, the predominant stem section that contributes to stem bending, and whether the effect of plant bending on force direction (stem reconfiguration) or relative velocity (stem velocity) is most important.

2.3. Wave damping

Dalrymple et al. (1984) showed that wave damping over a flat bottom is controlled by the conservation of wave power, which is given in its dimensionless form by

$$c_{g^*} \frac{\partial E_*}{\partial x_*} = -8 \lambda_f F_r^2 D^{-1} \varepsilon_{v^*} \tag{12}$$

where $E_* = H_*^2$ is the wave energy and $c_{g^*} = \frac{1}{2k_*} + \frac{D}{\sinh 2k_* D}$ is the wave

group velocity. We have introduced $\lambda_f = n_v b_v h_v$ as the frontal area per unit ground area (Britter and Hanna, 2003; Lowe et al., 2005), $F_r = u_c/\sqrt{gh}$ as the Froude number, $D = h/A_w$ as the ratio between water depth and wave excursion, and $k_* = kA_w$ as the dimensionless wave number. Furthermore, ε_{v*} is the energy dissipation per stem due to the work done by wave forces given by

$$\varepsilon_{v*} = \int_{s_*=0}^{1} \overline{F_{D*} \cdot U_{s*}}\, ds_*. \tag{13}$$

Here the overbar denotes phase-averaging over a wave cycle. Although F_{A*} and F_{FK*} can be of sufficient magnitude to control plant motion, they act out of phase with the water motion such that their phase-averaged work done is considered to be negligible. This argument strictly requires that the phase difference between U_{s*} and u_{m*} is small, which is reasonable given that the phase difference between water and stem motion reduces when vegetation velocities increase (Mullarney and Henderson, 2010). Finally, we will employ

$$W_* = F_* \cdot U_{s*} \tag{14}$$

as a short-hand notation for the time-dependent work (W_*) done by waves per unit stem length.

The solution of Eq. (12) in terms of wave height expresses a decay in the direction of wave propagation. In case of rigid vegetation, Dalrymple et al. (1984) showed that the solution in terms of wave damping is given by

$$H_* = \frac{H_{0*}}{1 + \beta_* x_*}, \tag{15}$$

Where H_{0*} is the incident wave height and β_* is the damping coefficient, scaled as $\beta_* = \beta A_w$. In case of flexible vegetation, Eq. (15) holds when the vegetation dynamics remain constant, i.e. u_{m*} damps proportionally to H_*. This is assumed to be the case in this study given that the vegetation fields in our experiments and validation cases are short with a length of 1.5 m and up to 40 m respectively.

3. Wave damping analysis under observed plant motion

3.1. Laboratory experimental setup

Experiments of wave damping over rigid and flexible vegetation canopies were conducted in the wave flume of the Coastal Laboratory of Swansea University, UK, to identify key mechanisms in the wave-vegetation interaction. The wave flume measured 30.7 m in length, 0.8 m in width and 1.2 m in height. It had a piston-type wavemaker with active wave absorption at one end and a parabolic wave damper of reticulated foam at the other end (Fig. 2a). We measured the wave height, the water particle velocity field and the plant motion simultaneously. By observing plant motion, we avoid solving the force balance (Eq. (11)) as a requirement for calculating wave-induced forces (Eqs. (6)–(8)).

Cylindrical rigid and flexible mimic canopies were fixed on the floor of the wave flume. The two stem types differed only in flexural rigidity. Rigid vegetation was created from bamboo dowels with $EI_v = 9.0 \pm 4 \times 10^{-2}$ Nm^2 (mean $\pm$ standard deviation, measured using three-point bending testing). Silicon sealants were used to construct flexible vegetation with $EI_v = 1.7 \pm 0.3 \times 10^{-5}$ Nm^2. All stems were 300 mm in height and had a diameter of 5 mm. Stems were aligned in a staggered formation to form a canopy with a length of 1.5 m and a stem density of 1111 stems/m^2. A 90 mm wide section was cleared near the downstream edge of the canopy for velocity measurements at 1.35 m from the upstream edge of the vegetation field.

The vegetation patches were subjected to regular waves with variation in height, period, and water depth. The wave height varied between 0.08 and 0.20 m, the wave period between 1.4 and 2.0 s, and water depth between 0.30 and 0.60 m. The 24 test conditions (Table 1) were selected to represent a range of wave intensities. Each condition was run

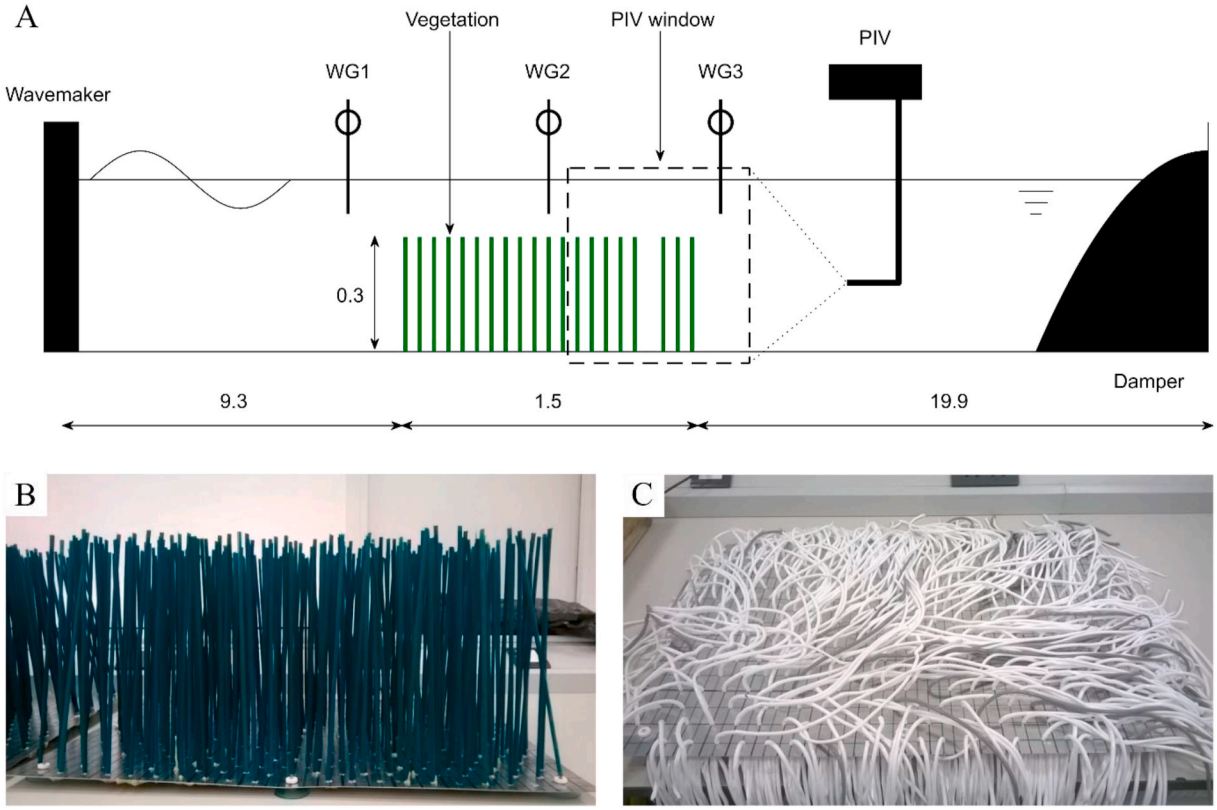

Fig. 2. (A) Sketch of the experimental set-up. All dimensions are in metres. Figure is not to scale; (B) Artificial rigid vegetation; (C) Artificial flexible vegetation.

Table 1
List of tested wave conditions and damping coefficients for rigid and flexible vegetation. u_c is derived from measured velocities according to Eq. (3). The width of the 95% CI of β_{exp} is given in brackets after its value. * Based on 2 instead of 3 runs; † Based on 1 run; Data quantity was reduced by control runs (u_c, rigid), or instrument malfunctioning. ‡ Plant motion not captured due to a moving floor plate.

CaseCase	H [m]H [m]	T [s]T [s]	h [m]h [m]	Rigid vegetation				Flexible vegetation			
				u_c [m/s]	Ca	L	β_{exp} [10^{-3}/m]	u_c [m/s]	Ca	L	β_{exp} [10^{-3}/m]
R1	0.15	1.4	0.60	0.13†	0.02	11	42 (6)	0.15	178	8.9	20 (9)*
R2	0.15	1.6	0.60	0.15*	0.04	7.6	38 (4)	0.19	278	6.2	16 (3)*
R3	0.15	1.8	0.60	0.17*	0.04	6.3	49 (9)	0.20	326	5.1	23 (5)*
R4	0.15	2.0	0.60	0.18*	0.05	5.3	42 (16)	0.22*	390	4.2	15 (16)*
R5	0.10	1.8	0.60	0.11*	0.02	9.2	39 (8)	0.14	146	7.6	20 (8)*
R6	0.20	1.8	0.60	0.21*	0.07	4.9	63 (9)	0.25	498	4.1	26 (19)*
R11	0.15	1.4	0.50	0.17*	0.04	7.9	72 (10)	0.19	271	7.2	21 (7)
R12	0.15	1.6	0.50	0.20*	0.06	6.0	67 (8)	0.21	352	5.5	17 (8)*
R13	0.15	1.8	0.50	0.20*	0.06	5.2	80 (18)	0.23	411	4.6	32 (6)
R14	0.15	2.0	0.50	0.22*	0.08	4.2	70 (30)	0.25	472	3.8	24 (12)
R15	0.10	1.8	0.50	0.14*	0.03	7.4	59 (18)	0.16	191	6.7	26 (5)
R16	0.20	1.8	0.50	0.26*	0.10	4.1	94 (22)	0.30	692	3.5	25 (15)
R21	0.15	1.4	0.40	0.20*	0.06	6.9	145 (23)	0.23	397	6.0	27 (15)
R22	0.15	1.6	0.40	0.21*	0.07	5.5	125 (13)	0.25	507	4.6	28 (13)
R23	0.15	1.8	0.40	0.22*	0.07	4.8	138 (9)	0.27	556	3.9	22 (9)*
R24‡	0.15	2.0	0.40	0.23*	0.08	4.1	108 (4)	0.25	498	3.7	48 (10)
R25	0.10	1.8	0.40	0.16*	0.04	6.7	97 (7)	0.18*	240	6.0	22 (12)*
R26	0.12	1.8	0.40	0.18*	0.05	5.8	116 (9)	0.21*	355	4.9	32 (14)*
R31	0.10	1.4	0.30	0.16*	0.04	8.6	210 (19)	0.18	266	7.3	56 (16)
R32	0.10	1.6	0.30	0.16*	0.04	7.3	219 (32)	0.20	309	5.9	68 (28)
R33	0.10	1.8	0.30	0.18*	0.05	5.9	197 (9)	0.21	333	5.1	62 (19)
R34	0.10	2.0	0.30	0.17*	0.04	5.6	195 (9)	0.20	325	4.6	62 (9)
R35	0.08	1.8	0.30	0.14*	0.03	7.5	169 (6)	0.17	238	6.0	51 (20)
R36	0.12	1.8	0.30	0.20*	0.06	5.3	219 (27)	0.24	444	4.4	40 (11)

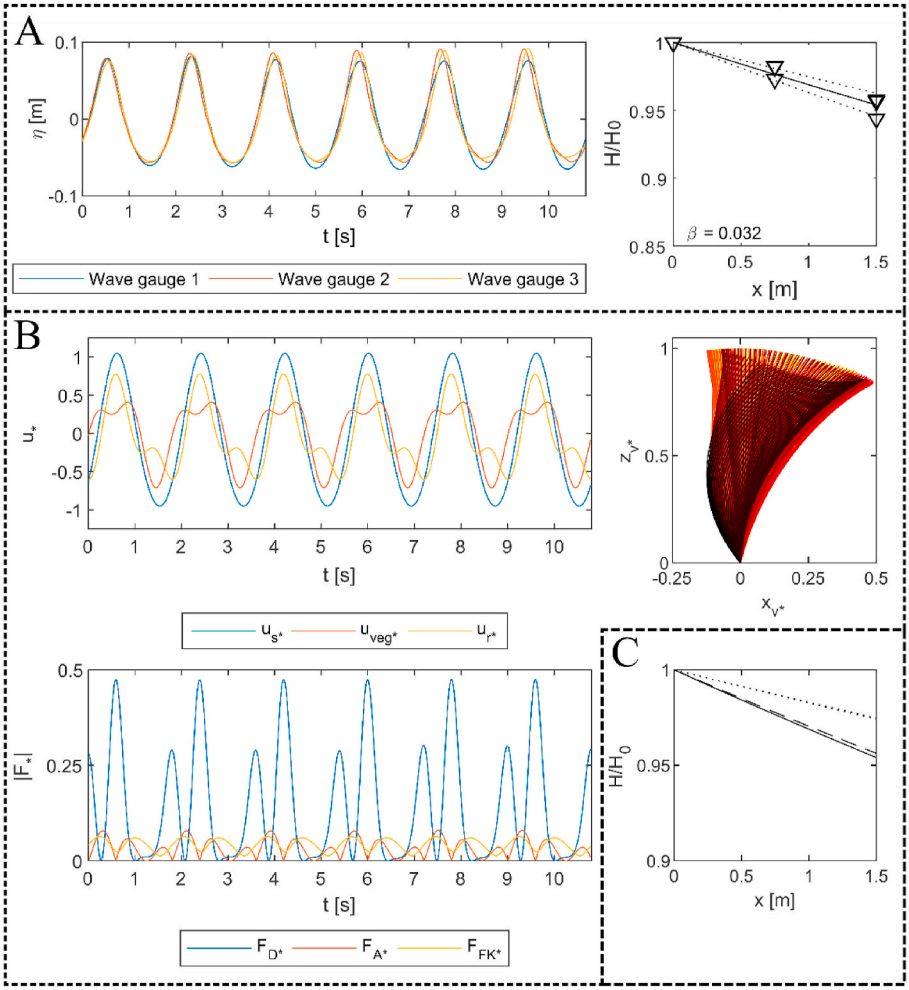

Fig. 3. Schematisation of the data collection from (A) wave gauges and (B) PIV, and (C) comparison of β under conditions R13 with flexible vegetation. Top left: time series of the water surface elevation as measured by the three wave gauges and corrected for phase differences. Top right: the data of the three repeats (triangles, some data points are overlapping) is combined to fit β_{exp} (solid line) with 95% confidence interval (dotted lines). Middle left: PIV derived horizontal particle velocities, vegetation velocity and relative velocity at $s_* = 0.5$. Middle right: PIV-derived plant motion. The colouring denotes the time and ranges from yellow (start of run) to black (end of run). Bottom left: Magnitudes of the wave forces at $s_* = 0.5$. Bottom right: Comparison of the force-derived β_{for} (dashed line) with β_{exp} (solid line). The dotted lines (only one is visible due to overlapping) denote β_{for} of the other repeats of R13. (For interpretation of the references to colour in this figure legend, the reader is referred to the Web version of this article.)

three times as reflection limited the number of undisturbed waves per run to 3–12 (Fig. 3a, left), which included a control run with reversed vegetation field to verify that the gap in the canopy did not affect wave dynamics. Although wave input was monochromatic, second order Stokes waves were observed due to shallow water conditions (Le Méhauté, 1976). Videos of the wave-vegetation interaction under conditions R3, R13, R23 and R33 can be found in the supplementary materials.

Wave heights were measured using three resistance type wave gauges (HR Wallingford, accuracy ± 0.1 mm). They were located upstream (WG1, 8.2 m downstream of the wave paddle), halfway (WG2, 10.0 m) and downstream (WG3, 10.8 m) of the vegetation patches. Wave measurements started when the water level had reached 95% of the incident wave amplitude and at least five waves had passed, and were terminated when the first reflected wave would reach the vegetation field based on shallow water wave theory. A single damping coefficient β_{exp} was fitted to Eq. (15) via the least-squares method using combined data of all three runs, providing 5 degrees of freedom (Fig. 3a, right). The damping coefficients of each condition and their confidence intervals are provided in Table 1. The average width of the 95% confidence interval (CI) of β_{exp} was 0.013 m^{-1} for rigid vegetation and 0.012 m^{-1} for flexible vegetation. The observed wave damping was significant with at least 3.3 mm for each condition, far exceeding the measurement error (0.1 mm). Furthermore, β_{exp} exceeded the width of the 95% CI for all but one test case (R4, flexible). It was verified through control runs that the damping over the flume floor was negligible ($\beta < 0.005$).

Water particle velocity fields inside and around vegetation were measured using Particle Image Velocimetry (PIV; Dantec systems). Polyamide seeding particles that follow water motion were added to the wave flume. These were tracked by a high-speed camera under laser illumination. The raw velocity field time series was obtained by cross-correlation of particle positions over consecutive camera frames. Following Luhar and Nepf (2016), a Fourier filter was applied to remove noise from the raw velocity time series. We retained only the wave-averaged velocities, the natural harmonic and the first higher order harmonic (Fig. 3b). The velocity time series aligned closely to the wave time series but were restricted to 11s due to the limitations on the number of frames that can be captured by the PIV-camera each run.

The velocity at rigid stems was derived from the water particle velocities inside the canopy. The velocity structure was considered fully developed as the gap was more than five drag length scales (Lowe et al., 2005) downstream of the canopy edge. The control runs with reversed vegetation prevented velocity measurements for one run per condition. Alternatively, the velocity at flexible stems was derived from the vertical velocity structure at the downstream edge for which stem motion can be identified simultaneously. Based on comparisons with control runs without vegetation, we found that flexible vegetation did not disturb the flow velocity structure apart from damping proportional to the wave height. Hence, the wave-vegetation interaction at the downstream edge is assumed to be representative for the whole canopy when velocity damping is accounted for.

Wave-averaged currents were observed within rigid vegetation canopies but not within flexible canopies. These observations agree with the velocity structures as proposed in Pujol et al. (2013). However, Luhar et al. (2010) and Abdolahpour et al. (2017) also observed wave-driven currents within flexible vegetation canopies. Their experiment setup differed significantly from ours as they used blades instead of cylinders. Furthermore, their experiments considered different wave conditions, longer canopies (L_v = 3-9 m) and increased test durations (6–10 min), which may have promoted flow convergence. Yet, Pujol et al. (2013) did not observe wave-driven currents through flexible canopies over equally long timeframes. Also, our canopy length and test duration sufficed for the development of currents through rigid vegetation. Given the contrasting observations and conditions, future research in this topic and its effect on plant motion and associated wave damping is advised.

Plant motion of flexible vegetation was derived from the frames captured by the PIV-camera through fitting a circular arc between the tip and the root for each frame (Fig. 4). We assume stem inextensibility such that the arc length equals vegetation height, and downstream bending as this is the dominant direction under extreme motion (Rupprecht et al., 2017). Under these assumptions, the stem position has a unique solution when the chord length d between the tip and the root satisfies $1 > d/h_v \geq 2/\pi$ (Fig. 4a). If $d = h_v$, a straight stem between root and tip is fitted (Fig. 4b). Finally, a circular arc cannot be fitted when $d/h_v < 2/\pi$, which may occur under extreme bending. The smallest semi-circle with diameter $d = 2h_v/\pi$ is fitted instead (Fig. 4c). Tip positions of a stem at the downstream edge of the patch have been identified manually for each frame by two independent controllers (Fig. 4d). This was found to be more accurate than automatic identification due to the variation in illumination and the low contrast between stems in the canopy. It is noted that a circular arc may not accurately represent stem configurations with two inflection points nor configurations with an arc angle greater than that associated with a semicircle, but it does accurately represent the motion of the tip which sways the most as it is identified directly. Additionally, the errors in plant posture may have a limited impact on wave damping as we will show in the following sections. An example of the computed plant motion is included in Fig. 3b. Full videos of derived plant motion are included in the supplementary materials.

The observed plant motion ranged from straight stems to fully flattened canopies. Plant motion developed during the measurement period with 25% of the runs exhibiting a change in maximum bending angle of more than 10°. It is expected that this affected the measured wave damping and the wave forces equally. The vegetation velocity is derived numerically trough a central difference scheme on the plant configuration. Following the derivation of water particle velocities, we have applied a Fourier filter to retain only the natural and first order harmonics of the vegetation velocity.

The wave-induced forces are computed based on the velocity signal and plant motion, according to Eqs. (6)–(8) (Fig. 3B). Then, the force-derived damping coefficients β_{for} was solved numerically through substitution of Eq. (15) in Eq. (12) (Fig. 3C). This produces a third-order polynomial function which may provide three instead of one solution for β_{for}. In these instances, the β_{for} which is closest to β_{exp} is selected. β_{for} successfully reproduces the wave damping over flexible vegetation an order of magnitude smaller than over rigid vegetation with goodness-of-fit $r^2 = 0.84$ (Fig. 5), using a drag coefficient that was derived for rigid vegetation. This shows that explicitly including the plant motion effect in the drag force (Eq. (6)) can explain the reduction in wave damping by flexible vegetation.

Whilst the confidence interval in β_{exp} has been quantified from the water surface measurements, this was not possible for β_{for}. Therefore, we address the individual sources of error in β_{for}, namely: the C_d-relation (Eq. (9)), the velocity measurements, and the plant motion. Eq. (9) was fitted with a goodness-of-fit of $r^2 = 0.89$ (Hu, pers. comm.), but a confidence interval is not known. The normalized standard deviation of the measured velocity amplitude (Eq. (2)) at identical water depth and vegetation type varied between 0.02 and 0.08 (van Veelen et al., 2020). Thirdly, the normalized standard deviation of the vegetation velocity ranged between 0.12 and 0.25 at the tip. Each error propagates into β_{for}, which contributes to the scatter of data seen in Fig. 5. The normalized root-mean-square errors (NMRSE) of β_{for} with respect to β_{exp} are 0.39 and 0.50 for rigid and flexible vegetation respectively. Whilst the r^2 of our methodology is very good, the fit may improve further with data from additional wave gauges to estimate β_{exp} more accurately, or when the uncertainty by any of the model errors is mitigated which can be recommended for future studies.

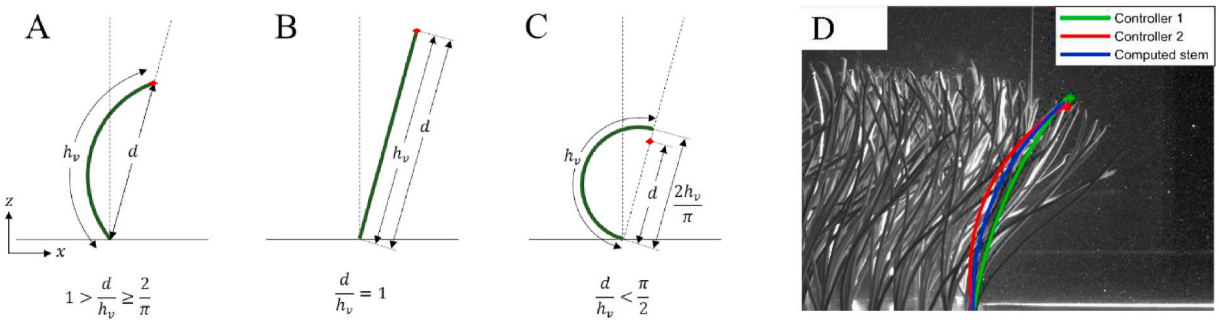

Fig. 4. Schematisation of the derivation of the plant position from a fixed root and identified tip position (red diamond) under three conditions: (A) a bent stem, (B) a straight stem and (C) extreme stem bending; and (D) application to a sample image. (For interpretation of the references to colour in this figure legend, the reader is referred to the Web version of this article.)

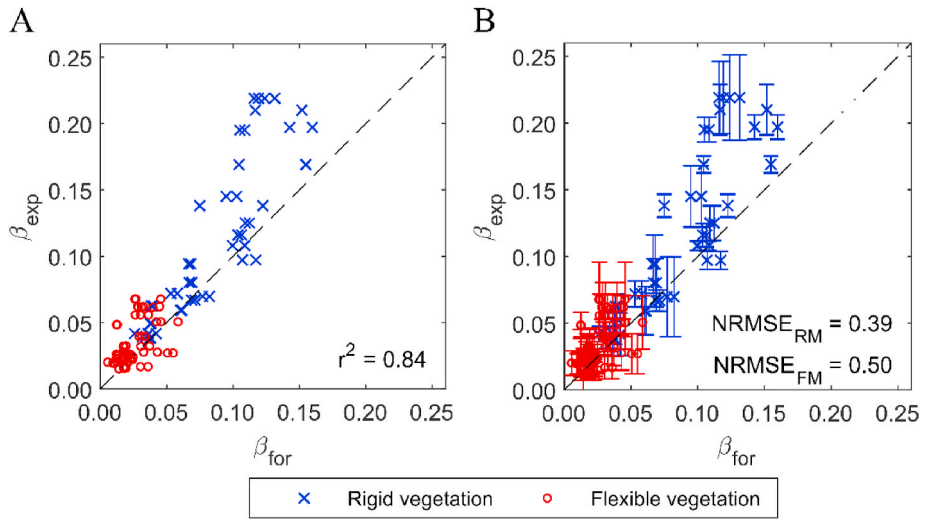

Fig. 5. (A) The correlation between the force-derived damping coefficient β_{for} and the measured damping coefficient β_{exp}, and (B) same as (A) with error bars that match the 95% confidence interval of β_{exp}.The normalized root-mean-square error (NRMSE) is given separately for the rigid (RM) and flexible (FM) mimics.

3.2. Key mechanisms in the wave-vegetation interaction

Force magnitudes: We find that the drag force is the dominant wave force on flexible vegetation but the added mass and Froude-Krylov forces increase in relative magnitude when plant motion increases at higher *Ca* and towards the tip of the stem (Fig. 6). The plant motion is limited at low *Ca* and at the bottom of the stem, where the motion is constrained by its root. When plant motion increases, the ratio $\pi^2/(KC|u_{rn^*}|)$ increases such that the magnitudes of F_{A^*} and F_{FK^*} increase relative to F_{D^*}. Our experimental results show that the root-mean-square magnitudes of F_{A^*} and F_{FK^*} are in the range of 15–20% of F_{D^*} at $s_* = 0.17$, 25–35% at $s_* = 0.5$, and 100% at $s_* = 0.83$. Although the relative magnitude of F_{A^*} and F_{FK^*} increases towards the tip, their magnitude remains low compared to the drag force exerted on the bottom section of the stem.

Distribution of wave energy dissipation: The distribution of energy dissipation versus stem length shows that most energy is dissipated where the stem is upright and its motion is minimal (Fig. 7). The

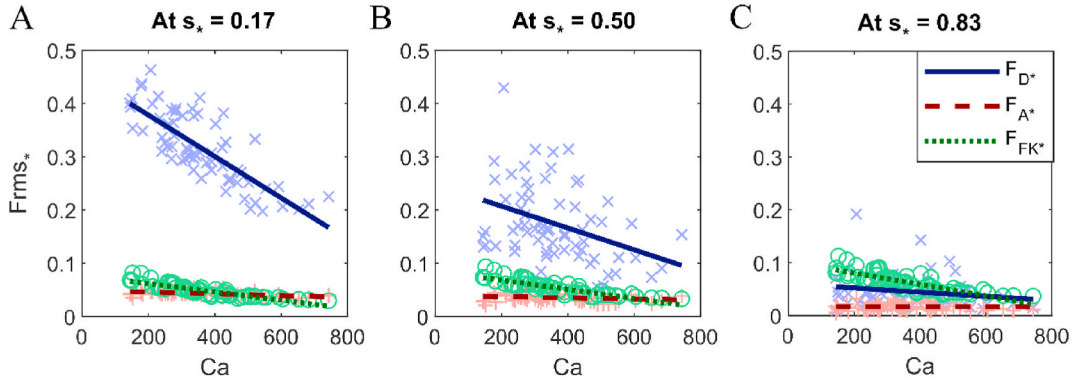

Fig. 6. Root-mean-square force magnitude of the drag force F_{D^*}, the added mass force F_{A^*}, and the Froude-Krylov force F_{FK^*} on flexible vegetation as function of the Cauchy number at (A) $s_* = 0.17$, (B) $s_* = 0.5$, and (C).$s_* = 0.83$.

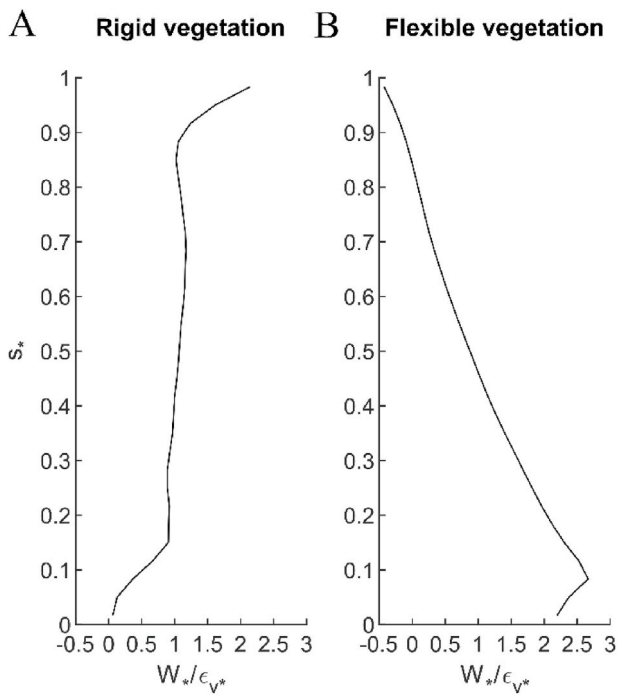

Fig. 7. Average rate of energy dissipation versus the along-stem coordinate for (A) rigid and (B) flexible vegetation.

dissipation over an upright rigid stem is approximately constant along its length with a peak in dissipation at the tip where amplified velocities were observed due to wave-driven currents through the top of the canopy (see e.g.,Abdolahpour et al., 2017; Pujol et al., 2013). Alternatively, the wave dissipation is concentrated at the bottom part of the stem for flexible vegetation with near-zero to negative contributions at the top section ($s_* > 0.7$). The decreasing contribution to energy dissipation over the stem length is inversely proportional to stem motion, which is absent at the fixed root and maximum at the tip.

Stem reconfiguration versus stem velocity: The swaying of flexible vegetation reduces wave damping in two ways. First, the reconfiguration of the stem posture reduces the stem frontal area (Paul et al., 2016) and modifies the direction of wave forces (Luhar and Nepf, 2016; Zeller et al., 2014). Second, stem velocity reduces the relative velocity between stem and water (e.g. Mendez and Loasada, 2004). Both mechanisms reduce the work done by the drag force but have not been quantified individually. To identify the dominant mechanism, we quantify ϵ_v by modifying Eq. (6) such that it solely includes stem reconfiguration or stem velocity. Wave damping by stem reconfiguration includes the directionality of the drag force relative to the stem, but the vegetation velocity is set at zero such that

$$F_{D_*} = \frac{1}{2} C_D |u_{n^*}| u_{n^*} e^{-i\theta} \tag{16}$$

with u_{n^*} as the stem-normal component of the water velocity. Alternatively, stem velocity includes the relative velocity in the force equations, but the stem is considered upright for the directionality of the forces, i.e.

$$F_{D_*} = \frac{1}{2} C_D |u_{r^*}| u_{r^*}. \tag{17}$$

Finally, we consider the rigid stem drag force which excludes both stem reconfiguration and stem velocity as a reference for the relative contribution of each mechanism. The rigid stem drag force is given by

$$F_{D_*} = \frac{1}{2} C_D |u_{s^*}| u_{s^*}. \tag{18}$$

The respective wave energy dissipations per stem are obtained according to Eq (13). The contributions of the bending (Eq. (16)) and relative velocity (Eq. (17)) to wave energy dissipation are scaled against the dissipation that is simulated by the full drag force equations (Eq. (6)) and the dissipation simulated by the rigid stem drag force (Eq. (18)).

Our results show that stem velocity is more important than stem reconfiguration. The inclusion of stem velocity explains 92.3% of the observed reduction in ε_v due to plant motion, whereas the individual contribution of the stem reconfiguration is 34.6% (Fig. 8). Thus, the stem velocity effect can explain almost all reduction in wave energy dissipation. Conversely, whilst stem bending can explain 34.6% of the reduction in wave energy dissipation individually, its added effect when the relative velocity is included is only 7.7%. These results fit with the concentration of energy dissipation at the lower section of the stem (Fig. 7), which is straighter than the top section. Stem bending is significant at the tip, but the contribution of the top section to wave energy dissipation is small.

4. Model for wave damping over flexible vegetation

4.1. Model assumptions

The key mechanisms in the wave-vegetation interaction justify our assumptions for modelling wave damping of regular waves over flexible vegetation. We assume that

1. Wave energy is dissipated where plant deflections are small and the plant posture is near-vertical;
2. The drag force controls the wave-vegetation interaction;
3. Stem-stem interactions can be neglected;
4. Vegetation is cylindrical with homogeneous cross-sections and flexural rigidity;
5. Stems are inextensible.

Assumption 1 is supported by the concentration of energy dissipation in the upright lower part of a flexible stem and the dominant contribution of the relative velocity mechanism relative to stem bending, as supported by our experiments. Assumption 2 follows from the obser-

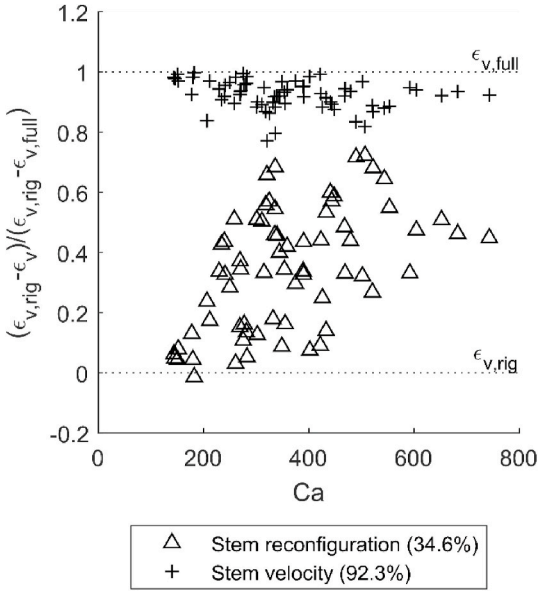

Fig. 8. Individual contributions of stem reconfiguration (based on Eq. (16)) and stem velocity (based on Eq. (17)) effects to the reduction in the wave energy dissipation. The average contribution of each effect is given between brackets. The contributions are scaled relative to the energy dissipations based on the full drag force (Eq. (6), upper dotted line) and the drag force based on a rigid stem (Eq. (18), lower dotted line).

vation that F_{A^*} and F_{FK^*} are an order of magnitude smaller than F_{D^*} in the bottom section of the stem which is key for wave damping. F_{A^*} and F_{FK^*} may be important at the top sections of a flexible stem but their magnitude remains an order of magnitude smaller than F_{D^*} in the bottom section. Assumptions 3–5 are required to derive the force balance (Eq. (11)), which was successfully applied to predict wave forces.

Our model assumptions reflect those in small excursion models as in Méndez et al. (1999) and Mullarney and Henderson (2010), who used Euler-Bernoulli beam theory to solve vegetation motion. Here we have provided new experimental support for this type of model, and our model differs in the extension of plant motion to wave damping. Scaling analysis shows that small excursion models are valid for $L \gg 1$ (Luhar and Nepf, 2016). Our experimental results ($L = 3$–9) show that the wave energy dissipation is concentrated at the bottom section of a stem where its velocity and excursion are low compared to the water velocity. This suggests that the model assumptions are valid for excursion ratios in the order $O(10^0)$. The model validation (Section 5.2) includes wave and vegetation conditions with L as low as 1.4 which covers most salt marsh ($L = 0.3$–10 (Rupprecht et al., 2017; van Veelen et al., 2020)) and sea grass ($L = 0.5$–6 (Lei and Nepf, 2019)) conditions. In case of $L < 1$, flexible vegetation may be fully extended, and the vegetation velocity may reduce to 0. Under these conditions, our model will provide a conservative estimate of the energy dissipation. Furthermore, we have considered vegetation conditions up to $Ca \approx 700$ in our experiments. The dominance of F_D on the bottom stem section is well established by our experimental evidence within this range, but may not be extrapolated to more flexible vegetation. The conditions $L > 1.4$ and $Ca < 700$ represent the quasi-flexible vegetation conditions for which our model will be validated. Finally, the model is derived for cylindrical vegetation but it can easily be extended to other plant geometries given appropriate relations for C_D and Ca.

4.2. Solution of plant motion

Under the model assumptions, vegetation motion is governed by horizontal stem excursion (x_{v^*}) which must satisfy the force balance (Eq. (11)) in the horizontal direction. For a near-vertical stem, it is appropriate to scale x_v by the horizontal water particle excursion length A_w rather than by plant length h_v as was done up to this point, i.e. $x_{v^*} = x_v/A_w$ and $u_{veg^*} = \partial x_{v^*}/\partial t_*$. Furthermore, the bending angle is approximated as $\theta \approx \partial x_{v^*}/\partial z_{v^*}$ and $s_* \approx z_{v^*}$ at this small-deflection limit (Luhar and Nepf, 2016; Mullarney and Henderson, 2010). We consider thin stems for which stem inertia is negligible ($\frac{1}{2}\frac{\pi^2}{KC}\rho' \ll 1$). Finally, the drag force, now given by Eq. (17), is linearised for the purpose of solving the force balance only. Under these conditions, Eq. (11) simplifies as

$$\frac{\partial^4 x_{v^*}}{\partial z_{v^*}^4} = Q\left(u_{s^*} - \frac{\partial x_{v^*}}{\partial t_*}\right) \tag{19}$$

where scaled flexibility $Q = \frac{4}{3\pi} C_D Ca L \int_0^1 (a_u - a_v) dz_{v^*}$ is the linearised parameterisation of the magnitude of drag force, and a_u and a_v are the amplitudes of the water and vegetation velocity respectively. Equivalent work is done over a wave cycle by the linearised drag as would be by quadratic drag (Méndez et al., 1999; Zimmerman, 1982). The boundary conditions of Eq. (19) are defined as clamped at the root, $x_{v^*} = \partial x_{v^*}/\partial z_{v^*} = 0$ at $z_{v^*} = 0$, and free at the tip, $\partial^2 x_{v^*}/\partial z_{v^*}^2 = \partial^3 x_{v^*}/\partial z_{v^*}^3 = 0$ at $z_{v^*} = 1$.

Wave and plant motion are periodic over a wave cycle and must satisfy the eigenvalue problem posed by Eq. (19). Therefore, we separate the motion quantities in a temporal mode following the monochromatic wave frequency and orthogonal spatial modes following the given eigenvalue problem (Mullarney and Henderson, 2010), according to

$$u_{s^*} = \Re\left(e^{it_*}\sum_{n=1}^{\infty} U_n\psi_n\right),\ u_{veg^*} = \Re\left(e^{it_*}\sum_{n=1}^{\infty} V_n\psi_n\right),\ x_{v^*} = \Re\left(e^{it_*}\sum_{n=1}^{\infty} X_n\psi_n\right). \tag{20}$$

The spatiotemporal complex coefficients U_n, V_n and X_n denote the weights of each mode in spectral space. The spatial modes ψ_n satisfy $\partial\psi_n/\partial z_{v^*} = \alpha_n\psi_n$ where α_n are the eigenvalues of each spatial mode. Further details regarding the structure of ψ_n are provided in Appendix A.

By substitution of Eq. (20) in Eq. (19) and summation over all spatial modes, we construct the transfer function $G = a_G e^{i\varphi_G}$ between the water and stem motion in physical space according to

$$V_f = GU_f \tag{21}$$

where $U_f(z_{v^*}) = \sum U_n\psi_n = a_u e^{i\varphi_u}$ and $V_f(z_{v^*}) = \sum V_n\psi_n = a_v e^{i\varphi_u}$ are complex temporal coefficients in physical space, and

$$G = \frac{\sum\left(\frac{U_n\psi_n}{1-\frac{ia_v^4}{Q}}\right)}{\sum U_n\psi_n}. \tag{22}$$

Here, a_G denotes amplitude transfer from water to stem motion and φ_G denotes the phase lag between water and stem motion. As Q is a function of a_v, Eq. (22) is solved iteratively. There is a unique solution as shown in Appendix B. The numerical implementation expands velocity structures to 10 spatial modes as additional modes did not change the resulting transfer function.

Additionally, we define the transfer function $R = a_R e^{i\varphi_R}$ between water velocity and relative velocity, i.e. $U_f - V_f = RU_f$. By substitution of this definition in Eq. (21), it follows

$$R = 1 - G. \tag{23}$$

4.3. Work factor (χ)

To include the effects of plant motion on energy dissipation, we define z_{v^*}-dependent work factor

$$\chi(z_{v^*}) = \frac{\overline{W}_*}{\overline{W}_{rig^*}}, \tag{24}$$

such that

$$\varepsilon_{v^*} = \int_{z_{v^*}=0}^{1} \chi\overline{W}_{rig^*}\, dz_{v^*}, \tag{25}$$

where $\overline{W}_*$ is the phase-averaged work done over a flexible stem and $\overline{W}_{rig^*}$ is the work done over a rigid stem with equal dimensions. By substitution of Eqs. (17) and (23) in Eq. (14), the phase-averaged work done by the drag force on a stem is given by

$$\overline{W}_* = \frac{1}{4\pi} C_D \int_{t_*=0}^{2\pi} \left|\Re\left(RU_f e^{it_*}\right)\right| \Re\left(RU_f e^{it_*}\right)\Re\left(U_f e^{it_*}\right) dt_*. \tag{26}$$

We note that $\Re(e^{it_*}) = \cos t_*$ and set $\varphi_u = -\varphi_R$ without loss of generality as W_* is averaged over a wave cycle. Then, Eq. (26) reduces to

$$\overline{W}_* = \frac{2}{3\pi} C_D a_R^2 a_u^3 \cos\varphi_R. \tag{27}$$

In case of rigid vegetation, $a_R = 1$ and $\varphi_R = 0$ as velocity transfer is absent, such that

$$\overline{W}_{rig^*} = \frac{2}{3\pi} C_D a_u^3 \tag{28}$$

and, by substitution of Eqs. (27) and (28) in Eq. (24),

$$\chi = a_R^2 \cos \varphi_R. \tag{29}$$

Eq. (29) shows how the velocity transfer controls wave damping. Changes in amplitude and phase of the relative velocity directly affect the work done by waves on vegetation and, thereby, the wave damping. Defining χ is computationally more efficient than computing the vegetation and relative velocity time series.

4.4. Wave damping

A formulation for wave damping coefficient β_* is obtained by substitution of Eqs. (15) and (25) in Eq. (12), which leads to

$$\frac{\beta_*}{(1+\beta_* x_*)^3} = 4\frac{\lambda_f F_r^2}{D c_{g*} H_{0*}^2} \int_{z_{v*}=0}^{1} \chi \overline{W}_{rig*}\, dz_{v*}. \tag{30}$$

Eq. (30) represents a third-order polynomial which is solved numerically. There may be up to three roots that satisfy Eq. (30), of which the root closest to the estimate by linear wave theory (Eq. (32), Section 4.5) is selected.

4.5. Wave damping under linear wave theory

When the validity of linear wave theory inside the canopy is assumed, the velocity structure is controlled by the ambient velocity field. The amplitude of the water particle velocities is given by

$$a_u(x_*, z_{v*}) = \frac{H_* k_*}{2F_r^2} \frac{\cosh L k_* z_{v*}}{\cosh D k_*}. \tag{31}$$

Substitution of Eqs. (15), (28) and (31) in Eq. (30) and application of the dimensionless dispersion relation $DF_r^2 = k_* \tanh(Dk_*)$ reduce the conservation of energy to a single expression for β_*, according to

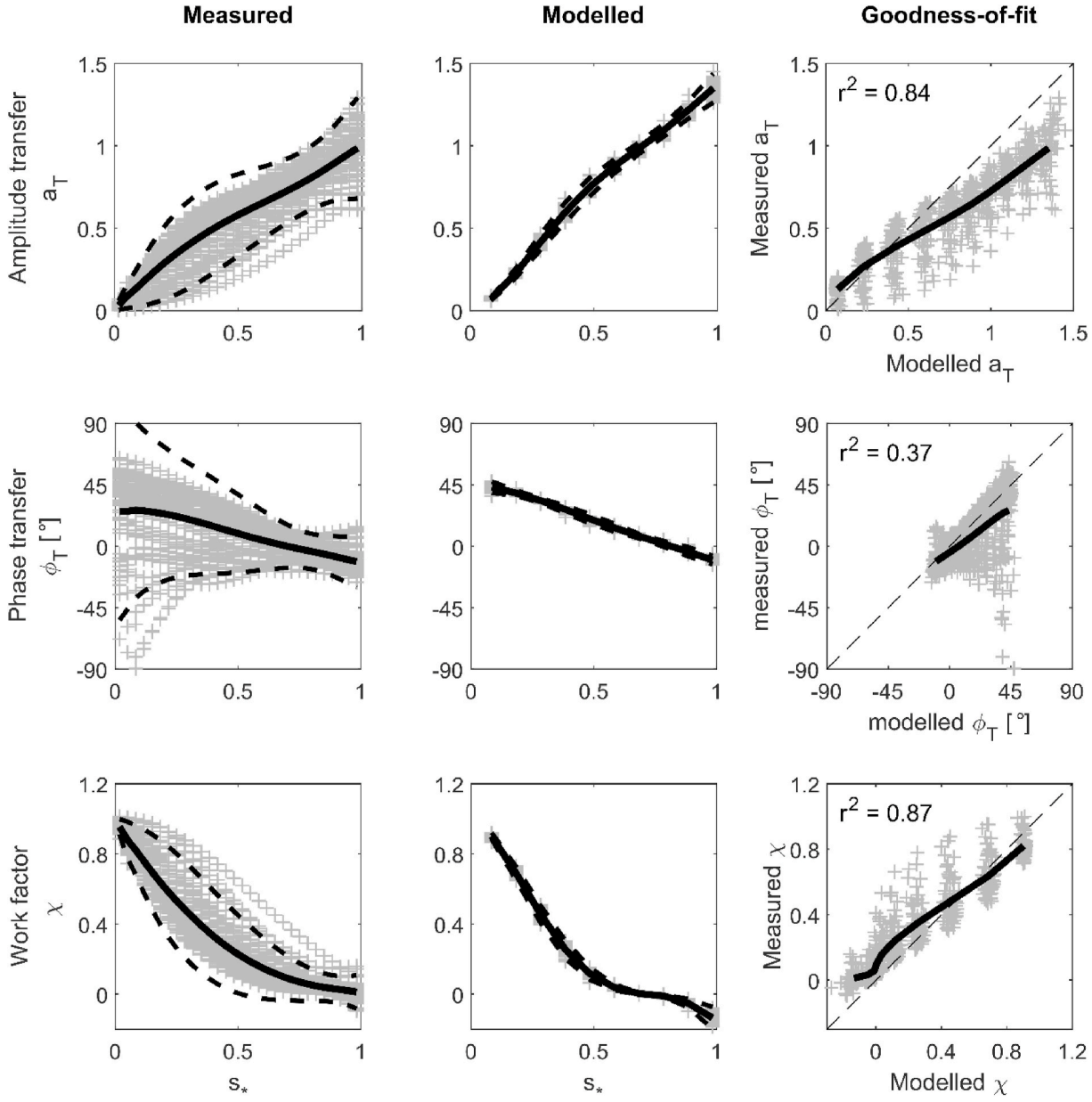

Fig. 9. Validation of the velocity transfer function between water and stem motion. Top row: amplitude transfer a_G; middle row: phase transfer φ_G; bottom row: work factor χ. The thick line denotes the mean of the measured (left column) or modelled (middle column) transfer functions, or the goodness-of-fit of the mean (right column). The dashed lines denote the 95% observation interval (mean ± 2 standard deviations; left and middle column), or the line of perfect fit (right column). The grey + signs represent the individual observations.

$$\beta_* = \frac{4}{3\pi} C_D \lambda_f D k_*^2 H_{0*} \frac{\int_{z_{v*}=0}^{1} \cosh^3(Lk_* z_{v*}) dz_{v*}}{(\sinh 2\,Dk_* + 2Dk_*)\sinh Dk_*}. \quad (32)$$

We note that for rigid vegetation, $\chi = 1$ and Eq. (32) reduces to the rigid vegetation solution provided in Dalrymple et al. (1984).

5. Model validation

5.1. Validation of the velocity transfer function (G)

The modelled velocity transfer function G is validated against a measured transfer function based on the observed water and plant motion. The measured transfer function is derived from the amplitude and phase differences in the natural harmonic of the observed water particle and stem velocities (Section 3.1). The validation includes flexible vegetation only, as the transfer function for rigid vegetation is trivial.

The amplitude a_G of the transfer function is excellently reproduced by the model (Fig. 9, top row). The amplitude transfer is $a_G \approx 0$ at the root where the stem is clamped and increases towards the tip to $a_G \approx 1$ for both measured and modelled transfer functions. This indicates that the tip closely follows the water motion and the relative velocity is small, which fits with observations that the energy dissipation is small at the tip. The coefficient of determination is excellent with $r^2 = 0.84$. The velocity transfer is slightly overpredicted at the tip where the assumption of a near-vertical stem affected only by the drag force may not hold. Additionally, the modelled transfer function is steady state, but the measured transfer function was still developing in a quarter of the runs. In these cases, the measured transfer function is lower than the steady-state function, which may also contribute to the over-prediction of the modelled transfer function at the tip. The transfer function at the bottom section of the stem which is important for wave damping is modelled correctly.

The phase φ_G is reproduced well for most experimental runs (Fig. 9, middle row). Both measured and modelled phases show that the stem velocities lead water motion by 45° at the root, which decreases towards the tip where the water motion leads stem motion by 10°. The scattering of experimental data is larger than predicted by the model due to natural variation in wave-vegetation interaction not captured by the model and measurement errors in water and vegetation motion. The scattering is maximum at the root where stem motion is minimal and, therefore, phase calculations are most sensitive to measurement errors. A limited number of outliers (10 out of 68 successful runs) impact the coefficient of determination negatively ($r^2 = 0.37$). Yet, a visual comparison shows that most data points are centred around the line of perfect fit.

Work factor χ is excellently reproduced by the model (Fig. 9, bottom row). The measured work factor is derived from the measured transfer function via Eq. (29). The work done by waves on a flexible stem at the root is equal to the work done on a rigid stem as denoted by $\chi = 1$ at $s_* = 0$. The work factor decreases as the amplitude transfer from water to stem motion increases from root to tip. Here, a negative χ indicates that the stem velocities locally exceed the water velocities and the relative velocity is fully out of phase with the water velocities. This behaviour agrees with Mullarney and Henderson (2010) who showed that the tip motion of flexible stems can exceed the water motion that forces it. The agreement between measured and modelled work factors is excellent with $r^2 = 0.87$.

5.2. Validation of the damping coefficient

Damping coefficient β is validated across five vegetation species with distinct biomechanical properties under medium and high energy wave conditions. These include wave damping by the rigid and flexible artificial vegetation (Section 3.1) and against three species of real salt marsh vegetation: *Spartina Anglica*, *Puccinellia Maritima* and *Elymus Athericus* (Fig. 10). These species differ in dimensions and flexural rigidity (Table 2) and have been tested under regular waves in large-scale flumes. The test conditions varied in water depth, wave height, wave period and stem density such that the model is validated across a wide range of wave and vegetation conditions.

S. Anglica and *P. Maritima* were tested in the Cantabria Coastal and Ocean Basin (CCOB) of the University of Cantabria, Spain (Lara et al., 2016; Losada et al., 2016; Maza et al., 2015). *S. Anglica* is a stiff plant with the largest diameter of the species tested. Alternatively, *P. Maritima* is a thin and flexible salt marsh grass. The experimental conditions featured medium water depths ($h = 0.4$ - 0.6 m) and wave heights ($H = 0.15$ - 0.20 m) at a range of wave periods ($T = 1.2$ - 2.2 s) and vegetation densities ($n_v = 430$ - 2436 stems/m^2).

E. Athericus was tested in the Grosser Wellenkanal (GWK) of Forschungszentrum Küste in Hannover, Germany (Möller et al., 2014; Rupprecht et al., 2017). *E. Athericus* is a thin and tall quasi-flexible salt marsh grass. A 40 m long vegetation field was submerged in deep water ($h = 2$ m) and subjected to medium and high energy wave conditions

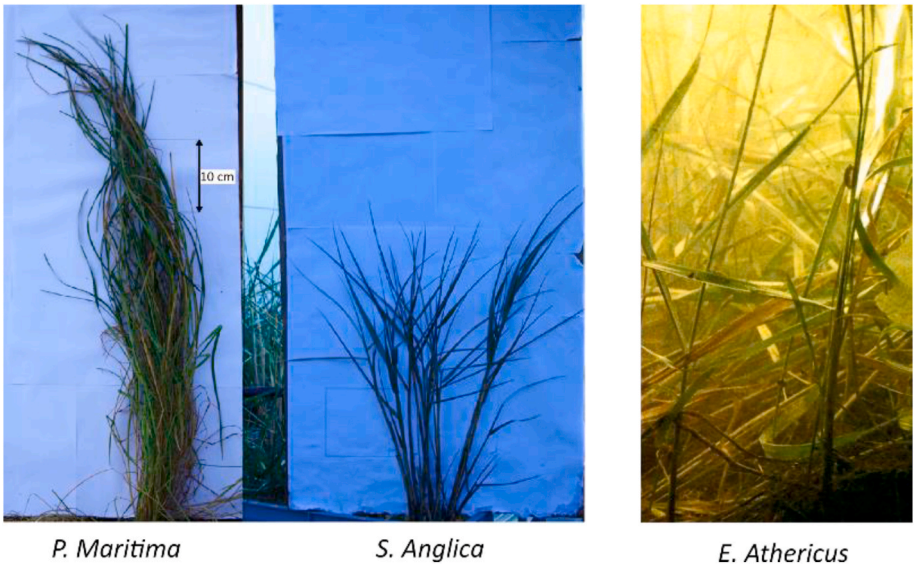

Fig. 10. The three real vegetation species that were used for model validation. Photo of P. Maritima and S. Anglica is adapted from Lara et al. (2016). Photo of E. Athericus is provided through the courtesy of Iris Möller (no scale available).

Table 2
List of vegetation species used for model validation. n denotes the number of unique wave conditions.

Parameter	Rigid mimics	Flexible mimics	*S. Anglica*[b]	*P. Maritima*[b]	*E. Athericus*[c]	Unit
Type	Artificial	Artificial	Real	Real	Real	–
h_v	300	300	284	473	700	mm
b_v	5.0	5.0	6.0	3.0	1.3	mm
EI_v	9.0×10^{-2}	1.7×10^{-5}	1.8×10^{-2}	8.7×10^{-5}	3.0×10^{-4}	Nm^2
n_v	1111	1111	430–729	877–2436	666–1225	m^{-2}
u_c	0.13–0.26	0.14–0.30	0.16–0.33	0.16–0.38	0.09–0.75	ms^{-1}
Ca	0.02–0.10	146–692	0.20–0.84	96–530	11–824	–
L	4.1–11	3.5–8.9	2.5–8.6	4.0–13	1.4–24	–
Q[a]	0.19–0.29	1013–1601	0.82–2.0	1041–2314	654–1656	–
n	24	24	14	18	10	–

[a] At first iteration, i.e. $a_v = 0$.
[b] Lara et al., 2016; Losada et al., 2016; Maza et al., 2015.
[c] Moller et al., 2014; Rupprecht et al., 2017.

($H = 0.11 – 0.89$ m, $T = 1.5$ - 5.1 s). The stem density decreased as the experiments progressed due to stem breaking. Therefore, the model was run following stem density data provided in Rupprecht et al. (2017).

The model is run with plant and wave conditions of individual runs as input. It is assumed that wave damping by real vegetation is dominated by the cylindrical stems. Fig. 10 shows that the geometry of the tested *S. Anglica* and *P. Maritima* species is dominated by their stems, and the tested *E. Athericus* was considered cylindrical in Rupprecht et al. (2017). The velocity fields around real vegetation are based on linear wave theory (Section 4.5), which was also successfully applied in the wave damping analysis in Losada et al. (2016) and Möller et al. (2014). The drag coefficient for all species is given by Eq. (9). The velocity scale is based on linear wave theory halfway based on measured wave height halfway the vegetation field as an estimate of the spatially averaged velocity. This non-predictive definition of the velocity scale can be avoided if the vegetation field is divided into sufficiently short sections, as is typically done when calculating vegetation-induced wave damping in large-scale computational wave models that use a gridded computational domain (e.g. SWAN (Booij et al., 1999)).

The agreement between modelled and measured wave damping is good with $r^2 = 0.66$ (Fig. 11), which shows that our model is applicable across a range of plant and wave conditions without plant-specific calibration. Excellent agreement is obtained for rigid and flexible artificial vegetation and for *E. Athericus*. The absence of vegetation motion is correctly modelled for rigid vegetation, as is the reduction in wave damping by flexible vegetation and *E. Athericus* due to plant swaying. Wave damping by *S. Anglica* and *P. Maritima* are predicted in the right order of magnitude but with significant scattering of the data, as demonstrated by their NRMSE of 0.56 and 0.62 respectively. This is partly attributed to the experiment setup of CCOB. Unlike rectangular flumes where vegetation spans the entire flume width, the CCOB features a circular platform on which vegetation is positioned. A circular vegetation patch may contribute to wave diffraction and other three-dimensional hydrodynamic effects, which are not included in our model. Furthermore, our omission of wave damping by leaves and stem-stem interactions may have contributed to an underestimation of the measured wave damping, as is observed for *P. Maritima*. Finally, buoyancy, added mass, and Froude-Krylov forces may have initiated a non-passive plant motion, which is not captured by our model and thus contributes to uncertainty in β_{model}.

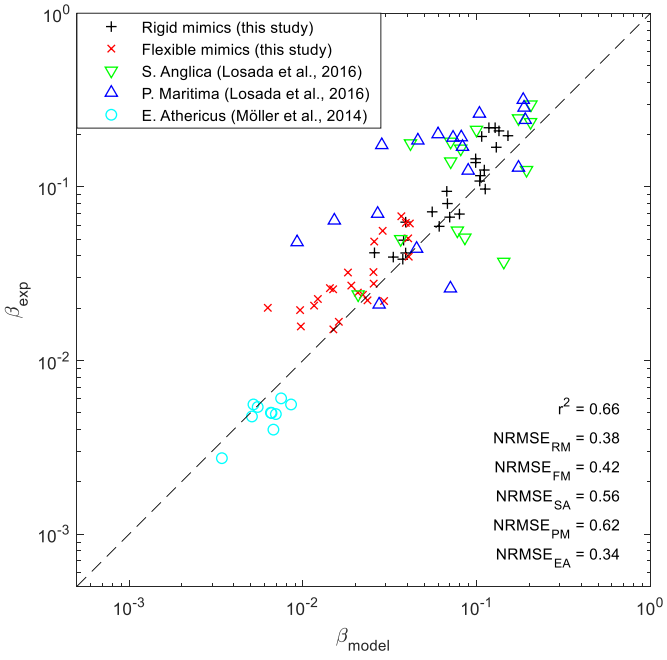

Fig. 11. Validation of the modelled wave damping coefficients β_{model} against the measured wave damping coefficients β_{exp} across two types of artificial vegetation and three species of real vegetation. The dashed line denotes a perfect fit. The r^2 goodness-of-fit is given, as well as the NMRSE of each specie. RM: Rigid mimics; FM: Flexible mimics; SA: S. Anglica; PM: P. Maritima; EA: E. Athericus.

6. Conclusions and discussion

We have developed a mathematical model for the damping of regular waves over coastal vegetation under quasi-flexible vegetation conditions, based on the key physical processes involved in the wave-vegetation interaction. Three mechanisms were identified during the experimental investigations as important for wave damping over rigid and flexible vegetation: (i) the drag force is the dominant force in the bottom section of a flexible stem; (ii) wave energy is dissipated in the bottom section of a flexible stem; (iii) wave energy dissipation is controlled by the velocity difference between water and stem rather than the reconfiguration of stem posture. We found that the energy dissipation by rigid stems was maximum at the stem tip where the wave velocities were the largest, while the dissipation by flexible stems was maximum at the upright bottom section where stem motion was the smallest.

Supported by our experimental investigations, we model vegetation as near-vertical flexible rods in which wave damping is controlled by the velocity transfer from water to stem motion. The velocity transfer is linked to a new work factor, which describes the reduction in wave dissipation relative to rigid vegetation due to plant motion. Wave damping in the model is a function of vegetation and wave parameters and does not require the calibration of the drag coefficient for different

plant species.

Our model successfully reproduces wave damping over vegetation for five coastal vegetation species, which differ in geometry and flexural rigidity, and under different wave climates. The model validation included three real vegetation species tested in large-scale experiments. Our model reproduced wave damping in the right order of magnitude for each specie and for both medium and high energy wave conditions, which shows its validity across a wide range of representative field conditions.

As our model does not require site-specific calibration, it is particularly suited to areas with spatiotemporal variations in vegetation and hydrodynamic conditions. It benefits large areas or areas where interventions such as managed realignment, grazing, and the introduction of new species are considered. Furthermore, the model can be applied to vegetation of different types, sizes and flexibilities when the plant geometry can be represented as a cylinder.

Despite the potential of our model shown in this research, it is important to emphasize the potential limitations that should be considered in the application of this model. First, the model assumptions rely on the experimental investigations, which limits their applicability to the quasi-flexible vegetation conditions considered in this study, i.e. $L > 1.4$ and $Ca < 700$. These conditions are applicable to most coastal vegetation species, but may be exceeded for very flexible species and during extreme wave conditions. Secondly, wave-vegetation mechanisms like vegetation-induced currents and inertia forces have been omitted in our modelling framework as they were not identified as key processes for wave damping in our experimental vegetation types. Our aim has been to develop a computationally fast model that balances complexity and applicability, justifying our focus only on key mechanisms. However, the selected key processes have been based on a specific set of experiments, which for example showed a negligible impact of wave-induced currents within flexible vegetation canopies as opposed to other experimental studies (Abdolahpour et al., 2017; Luhar et al., 2010). Although inertia forces have been included in other wave damping models (Luhar and Nepf, 2016; Maza et al., 2015), we found that they only had limited impact on wave damping in our experiments. Finally, the impact of leaves and stem-stem interactions were not considered in this study. Their influence on wave damping remains an open question.

Finally, our model builds strongly on our experimental data although we validated wave damping against independent datasets found in literature with real vegetation. The strong tie between experimental work and modelling means that uncertainties in model observations may propagate into model simulations. The main uncertainties in the experimental work are the relatively short canopy, wave reflection in the wave channel, and a simplified method used to visualise vegetation motion. The canopy of 1.5 m meant that only three wave gauges could be fitted around the vegetation, which limited the number of data points that could be used to fit β_{exp} and determine its accuracy. Additionally, the reflection in the wave tank limited the number of waves that could be used for the analysis. Finally, simplifying the vegetation postures to an arc meant that postures with a double infliction point or extreme bending could not be replicated. To reduce the impact of these uncertainties, each condition was repeated three times to increase data quantity and the final model was validated against two independent data sets with real vegetation fields. Nevertheless, the limitations of our experimental approach should be considered when applying our model. We recommend that our key mechanisms and wave damping predictions will be further validated with new independent datasets across a range of wave and vegetation conditions to enhance the predictive capacity of our model.

CRediT authorship contribution statement

Thomas J. van Veelen: Conceptualization, Methodology, Investigation, Validation, Formal analysis, Writing - original draft. **Harshinie Karunarathna:** Conceptualization, Methodology, Writing - review & editing, Supervision. **Dominic E. Reeve:** Resources, Writing - review & editing, Supervision.

Declaration of competing interest

The authors declare that they have no known competing financial interests or personal relationships that could have appeared to influence the work reported in this paper.

Acknowledgements

We thank Dr. J.M. Horrillo-Caraballo, Dr. T.S. Orimoloye and Dr. A. A. Zuhaira of Swansea University, for their invaluable assistance during the laboratory experiments. Dr. Zhan Hu is thanked for providing insights on the interpretation of the CD-relation (Eq. (9)). Prof I. Möller is gratefully acknowledged for providing an image of E. Athericus. We are grateful to two anonymous reviewers whose comments have greatly improved the quality of this manuscript. TvV acknowledges support for his PhD by the College of Engineering of Swansea University. This research formed part of the Valuing Nature Programme (valuing-nature.net) which is funded by the Natural Environment Research Council, the Economic and Social Research Council, the Biotechnology and Biological Sciences Research Council, the Arts and Humanities Research Council and the Department for Environment, Food and Rural Affairs. This research was supported by the UK Research Councils under Natural Environment Research Council award NE/N013573/1, Title CoastWEB: Valuing the contribution which COASTal habitats make to human health and WEllBeing, with a focus on the alleviation of natural hazards.

Appendix A. Supplementary data

Supplementary data to this article can be found online at https://doi.org/10.1016/j.coastaleng.2020.103820.

Appendix A. Description of the spatial modes

The orthogonal spatial modes of the plant and water motion are given by

$$\psi_n(z_{v^*}) = (\cosh \alpha_n z_{v^*} - \cos \alpha_n z_{v^*}) + \frac{\cos \alpha_n + \cosh \alpha_n}{\sin \alpha_n + \sinh \alpha_n}(\sin \alpha_n z_{v^*} - \sinh \alpha_n z_{v^*}), \tag{A.1}$$

where eigenvalues α_n satisfy

$$\cosh(\alpha_n)\cos(\alpha_n) - 1 = 0. \tag{A.2}$$

The first three roots of Eq. A.2 are given by $\alpha_1 = 0.5969\pi$, $\alpha_2 = 1.4942\pi$, $\alpha_3 = 2.5002\pi$, and are approximated by $\alpha_n = (n - 0.5)\pi$ thereafter. The

spatial modes satisfy Eq. 19 and their spatial derivative is given by

$$\frac{\partial \psi_n}{\partial z_{v^*}} = \alpha_n \psi_n. \tag{A.3}$$

The four lowest order modes are shown in Fig. A.1a. The weights of the complex spatiotemporal coefficients of the water motion are obtained by solving the linear system

$$\psi_n U_n = U_f \tag{A.4}$$

where $U_f(z_{v^*})$ are the temporal coefficients of the water motion along the stem. To solve Eq. A.4, the wave motion along the stem is discretised following the number of modes considered, which is set at 10 in this study. A sample decomposition of a velocity profile based on linear wave theory by 10 spatial modes is plotted in Fig. A.1b. Furthermore, the resulting vegetation velocity profile of an artificial flexible stem under the sample forcing is shown in Fig. A.1c. While higher order modes will better represent input velocity profile near the bottom, their effect on the resulting vegetation velocity is negligible due to their high eigenvalues (α_n).

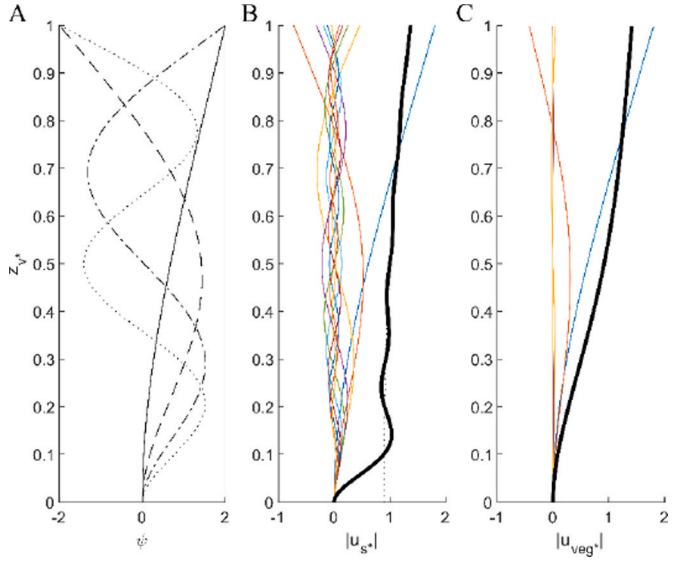

Fig. A.1. (A) The first four spatial modes ψ_n (Eq. A.1); (B) decomposition of a velocity structure given by linear wave theory into 10 spatial modes. The thin coloured solid lines denote the weighted spatial modes, the dotted black line denotes the input velocity profile and the thick black line denotes the sum of all spatial modes; (C) resulting vegetation velocity structure of the artificial flexible vegetation.

Appendix B. Proof of a unique solution of the velocity transfer function (T)

We substitute Eq. 21 and $Q = \frac{4}{3\pi} C_D CaL \int_0^1 (a_u - a_v) dz_{v^*}$ in Eq. 22. Furthermore, we consider the stem-averaged magnitude of both sides of Eq. 24 to obtain an expression for the stem-averaged vegetation velocity according to

$$\int_0^1 a_v dz_{v^*} = \int_0^1 \left| \sum \left(\frac{U_n \psi_n}{1 - \frac{U_n \psi_n}{i\alpha_n^4}} \right) \right| dz_{v^*}. \tag{B.1}$$

The stem-averaged magnitude of the vegetation velocity $\int_0^1 a_v dz_{v^*}$ is bound by $[0, \int_0^1 a_u dz_{v^*}]$. The lower bound denotes no vegetation motion and the upper bound represents full velocity transfer from water to vegetation motion. The left-hand side monotonically increases and the right-hand side monotonically decreases for increasing $\int_0^1 a_v dz_{v^*}$ within its range. Therefore, there is at most one solution of Eq. B.1.

We evaluate $\int_0^1 a_v dz_{v^*}$ at its lower and upper bound. If $\int_0^1 a_v dz_{v^*} = 0$, the left-hand side is smaller than the right-hand side of Eq. B.1. If $\int_0^1 a_v dz_{v^*} = \int_0^1 a_u dz_{v^*}$, then $Q = 0$ and the right-hand side of Eq. B.1 approaches 0. Yet $\int_0^1 a_v dz_{v^*} > 0$ at its upper bound when wave forcing is present. Thus, the left-hand side is larger than the right-hand side at the upper bound. As both sides of Eq. B.1 are continuous functions of $\int_0^1 a_v dz_{v^*}$, there is at least one solution of Eq. B.1. As we showed before that there is at most one solution, there must be exactly one solution of Eq. B.1 and Eq. 22.

References

Abdolahpour, M., Hambleton, M., Ghisalberti, M., 2017. The wave-driven current in coastal canopies. J. Geophys. Res. Oceans. 122, 3660–3674.

Anderson, M.E., Smith, J.M., 2014. Wave attenuation by flexible, idealized salt marsh vegetation. Coast. Eng. 83, 82–92.

Augustin, L.N., Irish, J.L., Lynett, P., 2009. Laboratory and numerical studies of wave damping by emergent and near-emergent wetland vegetation. Coast. Eng. 56, 332–340.

Booij, N., Ris, R.C., Holthuijsen, L.H., 1999. A third-generation wave model for coastal regions: 1. Model description and validation. J. Geophys. Res. 104, 7649–7666.

Bouma, T.J., van Belzen, J., Balke, T., Zhu, Z., Airoldi, L., Blight, A.J., Davies, A.J., Galvan, C., Hawkins, S.J., Hoggart, S.P.G., Lara, J.L., Losada, I.J., Maza, M., Ondiviela, B., Skov, M.W., Strain, E.M., Thompson, R.C., Yang, S., Zanuttigh, B., Zhang, L., Herman, P.M.J., 2014. Identifying knowledge gaps hampering application of intertidal habitats in coastal protection: opportunities & steps to take. Coast. Eng. 87, 147–157.

Bradley, K., Houser, C., 2009. Relative velocity of seagrass blades: implications for wave attenuation in low-energy environments. J. Geophys. Res. Earth Surf. 114.

Britter, R.E., Hanna, S.R., 2003. Flow and dispersion in urban areas. Annu. Rev. Fluid Mech. 35, 469–496.

Chen, H., Ni, Y., Li, Y., Liu, F., Ou, S., Su, M., Peng, Y., Hu, Z., Uijttewaal, W., Suzuki, T., 2018. Deriving vegetation drag coefficients in combined wave-current flows by calibration and direct measurement methods. Adv. Water Resour. 122, 217–227.

Chen, H., Zou, Q.-P., 2019. Eulerian-Lagrangian flow-vegetation interaction model using immersed boundary method and OpenFOAM. Adv. Water Resour. 126, 176–192. https://doi.org/10.1016/j.advwatres.2019.02.006.

Dalrymple, R.A., Kirby, J.T., Hwang, P.A., 1984. Wave diffraction due to areas of energy dissipation. J. Waterw. Port, Coast. Ocean Eng. 110, 67–79.

Dean, R.G., Dalrymple, R.A., 1991. Water Wave Mechanics for Engineers and Scientists. World Scientific Publishing Company, Singapore.

Fagherazzi, S., Kirwan, M.L., Mudd, S.M., Guntenspergen, G.R., Temmerman, S., D'Alpaos, A., van de Koppel, J., Rybczyk, J.M., Reyes, E., Craft, C., Clough, J., 2012. Numerical models of salt marsh evolution: ecological, geomorphic, and climatic factors. Rev. Geophys. 50, RG1002.

Garzon, J.L., Maza, M., Ferreira, C.M., Lara, J.L., Losada, I.J., 2019. Wave attenuation by Spartina saltmarshes in the chesapeake bay under storm surge conditions. J. Geophys. Res. Oceans. 124, 5220–5243.

Henderson, S.M., 2019. Motion of buoyant, flexible aquatic vegetation under waves: simple theoretical models and parameterization of wave dissipation. Coast. Eng. 152, 103497.

Hu, Z., Suzuki, T., Zitman, T., Uittewaal, W., Stive, M., 2014. Laboratory study on wave dissipation by vegetation in combined current–wave flow. Coast. Eng. 88, 131–142.

Jadhav, R.S., Chen, Q., Smith, J.M., 2013. Spectral distribution of wave energy dissipation by salt marsh vegetation. Coast. Eng. 77, 99–107.

Keulegan, G.H., Carpenter, L.H., 1958. Forces on cylinders and plates in an oscillating fluid. J. Res. Natl. Bur. Stand. Res. Pap. 2857, 423–440.

Koftis, T., Prinos, P., Stratigaki, V., 2013. Wave damping over artificial posidonia oceanica meadow: a large-scale experimental study. Coast. Eng. 73, 71–83.

Lara, J.L., Maza, M., Ondiviela, B., Trinogga, J., Losada, I.J., Bouma, T.J., Gordejuela, N., 2016. Large-scale 3-D experiments of wave and current interaction with real vegetation. Part 1: guidelines for physical modeling. Coast. Eng. 107, 70–83.

Le Méhauté, B., 1976. An Introduction to Hydrodynamics and Water Waves, first ed. Springer-Verlag, Berlin Heidelberg.

Leclercq, T., de Langre, E., 2018. Reconfiguration of elastic blades in oscillatory flow. J. Fluid Mech. 838, 606–630.

Lei, J., Nepf, H., 2019. Wave damping by flexible vegetation: connecting individual blade dynamics to the meadow scale. Coast. Eng. 147, 138–148.

Leonardi, N., Carnacina, I., Donatelli, C., Ganju, N.K., Plater, A.J., Schuerch, M., Temmerman, S., 2018. Dynamic interactions between coastal storms and salt marshes: a review. Geomorphology 301, 92–107.

Losada, I.J., Maza, M., Lara, J.L., 2016. A new formulation for vegetation-induced damping under combined waves and currents. Coast. Eng. 107, 1–13.

Lowe, R.J., Koseff, J.R., Monismith, S.G., 2005. Oscillatory flow through submerged canopies: 1. Velocity structure. J. Geophys. Res. Oceans 110.

Luhar, M., Coutu, S., Infantes, E., Fox, S., Nepf, H.M., 2010. Wave-induced velocities inside a model seagrass bed. J. Geophys. Res. Oceans. 115.

Luhar, M., Infantes, E., Nepf, H., 2017. Seagrass blade motion under waves and its impact on wave decay. J. Geophys. Res. Oceans. 122, 3736–3752.

Luhar, M., Nepf, H.M., 2011. Flow-induced reconfiguration of buoyant and flexible aquatic vegetation. Limnol. Oceanogr. 56, 2003–2017.

Luhar, M., Nepf, H.M., 2016. Wave-induced dynamics of flexible blades. J. Fluid Struct. 61, 20–41.

Maza, M., Lara, J.L., Losada, I.J., 2013. A coupled model of submerged vegetation under oscillatory flow using Navier–Stokes equations. Coast. Eng. 80, 16–34.

Maza, M., Lara, J.L., Losada, I.J., Ondiviela, B., Trinogga, J., Bouma, T.J., 2015. Large-scale 3-D experiments of wave and current interaction with real vegetation. Part 2: experimental analysis. Coast. Eng. 106, 73–86.

Mendez, F.J., Losada, I.J., 2004. An empirical model to estimate the propagation of random breaking and nonbreaking waves over vegetation fields. Coast. Eng. 51, 103–118.

Méndez, F.J., Losada, I.J., Losada, M.A., 1999. Hydrodynamics induced by wind waves in a vegetation field. J. Geophys. Res. Oceans. 104, 18383–18396.

Möller, I., Kudella, M., Rupprecht, F., Spencer, T., Paul, M., van Wesenbeeck, B.K., Wolters, G., Jensen, K., Bouma, T.J., Miranda-Lange, M., Schimmels, S., 2014. Wave attenuation over coastal salt marshes under storm surge conditions. Nat. Geosci. 7, 727–731.

Mullarney, J.C., Henderson, S.M., 2010. Wave-Forced motion of submerged single-stem vegetation. J. Geophys. Res. Oceans. 115.

Mullarney, J.C., Henderson, S.M., 2018. Flows within marine vegetation canopies. In: Panchang, V., Kaihatu, J. (Eds.), Adv. Coast. Hydraul. World Scientific, pp. 1–46.

Ozeren, Y., Wren, D.G., Wu, W., 2014. Experimental investigation of wave attenuation through model and live vegetation. J. Waterw. Port, Coast. Ocean Eng. 140, 04014019.

Paul, M., Rupprecht, F., Möller, I., Bouma, T.J., Spencer, T., Kudella, M., Wolters, G., van Wesenbeeck, B.K., Jensen, K., Miranda-Lange, M., Schimmels, S., 2016. Plant stiffness and biomass as drivers for drag forces under extreme wave loading: a flume study on mimics. Coast. Eng. 117, 70–78.

Pujol, D., Serra, T., Colomer, J., Casamitjana, X., 2013. Flow structure in canopy models dominated by progressive waves. J. Hydrol 486, 281–292.

Riffe, K.C., Henderson, S.M., Mullarney, J.C., 2011. Wave dissipation by flexible vegetation. Geophys. Res. Lett. 38, L18607.

Rupprecht, F., Möller, I., Paul, M., Kudella, M., Spencer, T., van Wesenbeeck, B.K., Wolters, G., Jensen, K., Bouma, T.J., Miranda-Lange, M., Schimmels, S., 2017. Vegetation-wave interactions in salt marshes under storm surge conditions. Ecol. Eng. 100, 301–315.

Schulze, D., Rupprecht, F., Nolte, S., Jensen, K., 2019. Seasonal and spatial within-marsh differences of biophysical plant properties: implications for wave attenuation capacity of salt marshes. Aquat. Sci. 81, 65.

Stark, J., Plancke, Y., Ides, S., Meire, P., Temmerman, S., 2016. Coastal flood protection by a combined nature-based and engineering approach: modeling the effects of marsh geometry and surrounding dikes. Estuar. Coast Shelf Sci. 175, 34–45.

Strusińska-Correia, A., Husrin, S., Oumeraci, H., 2013. Tsunami damping by mangrove forest: a laboratory study using parameterized trees. Nat. Hazards Earth Syst. Sci. 13, 483–503.

Sutton-Grier, A.E., Wowk, K., Bamford, H., 2015. Future of our coasts: the potential for natural and hybrid infrastructure to enhance the resilience of our coastal communities, economies and ecosystems. Environ. Sci. Pol. 51, 137–148.

Temmerman, S., Meire, P., Bouma, T.J., Herman, P.M.J., Ysebaert, T., De Vriend, H.J., 2013. Ecosystem-based coastal defence in the face of global change. Nature 504, 79–83.

van Veelen, T.J., Fairchild, T.P., Reeve, D.E., Karunarathna, H., 2020. Experimental study on vegetation flexibility as control parameter for wave damping and velocity structure. Coast. Eng. 157, 103648.

Vuik, V., Jonkman, S.N., Borsje, B.W., Suzuki, T., 2016. Nature-based flood protection: the efficiency of vegetated foreshores for reducing wave loads on coastal dikes. Coast. Eng. 116, 42–56.

Wamsley, T.V., Cialone, M.A., Smith, J.M., Ebersole, B.A., Grzegorzewski, A.S., 2009. Influence of landscape restoration and degradation on storm surge and waves in southern Louisiana. Nat. Hazards 51, 207–224.

Zeller, R.B., Weitzman, J.S., Abbett, M.E., Zarama, F.J., Fringer, O.B., Koseff, J.R., 2014. Improved parameterization of seagrass blade dynamics and wave attenuation based on numerical and laboratory experiments. Limnol. Oceanogr. 59, 251–266.

Zimmerman, J.T.F., 1982. On the Lorentz linearization of a quadratically damped forced oscillator. Phys. Lett. 89, 123–124.